RSC Advances

PAPER

View Article Online
View Journal | View Issue

Cite this: *RSC Adv.*, 2024, **14**, 1472

Directed assembly of fullerenols *via* electrostatic and coordination interactions to fabricate diverse and water-soluble metal cation–fullerene nanocluster complexes†

Rui He,‡[a] Chenjie Fan,‡[a] Qingyuan Liang,[a] Yan Wang,[a] Yanyan Gao,[a] Jiakai Wu,[a] Qingnan Wu*[a] and Fuju Tai *[b]

Metal ion–nanocluster coordination complexes can produce a variety of functional engineered nanomaterials with promising characteristics to enable widespread applications. Herein, the visualization observation of the interactions of metal ions and fullerene derivatives, particularly anionic fullerenols (**FoI**), were carried out in aqueous solutions. The alkali metal salts only resulted in salting out of **FoI** to gain re-soluble sediments, whereas multivalent metal cations (M^{n+}, $n = 2, 3$) modulated further assembly of **FoI** to produce insoluble hybrids. These provide crucial insights into the directed assembly of **FoI** that two major forces involved in actuation are electrostatic and coordination effects. Through the precise modulation of feed ratios of **FoI** to M^{n+}, a variety of water-soluble M^{n+}@**FoI** coordination complexes were facilely prepared and subsequently characterized by various measurements. Among them, X-ray photoelectron spectra validated the coordination effects through the metal cation and oxygen binding feature. Transmission electron microscopy delivered valuable information about diverse morphologies and locally-ordered microstructures at the nanoscale. This study opens a new opportunity for developing a preparation strategy to fabricate water-soluble metal cation–fullerenol coordination complexes with various merits for potential application in biomedical fields.

Received 12th November 2023
Accepted 13th December 2023

DOI: 10.1039/d3ra07725j

rsc.li/rsc-advances

1 Introduction

Metal ion–nanoscale cluster coordinated aggregation complexes have received great attention to produce a variety of functional engineered nanomaterials with promising characteristics of diverse architecture, great versatility, and applicability that have enabled a broad range of applications in materials science, energy, environment, and biomedicine,[1–3] including pollution restorers,[4,5] environmental purifiers,[6] batteries and solar cells,[7] catalysis,[8] artificial enzymes,[9] templating,[10] sensing,[11] anticancer drug delivery,[12] and theranostics.[13] As a few recent highlights, for example, the selected and precise coordination of a nanoscale polyoxometalate cluster with hexavalent actinides over trivalent lanthanides gave rise to a new ultrafiltration-based separation method for high-level waste in nuclear energy.[5] The synthetic use of electron-beam lithographic techniques induced the exceptional formation of an open-hole bimetallic lead–azafullerene complex to provide a new horizon for designing advanced and well-defined carbon nanostructures.[10]

Since the first discovery of fullerenes in 1985,[14] the insertion into carbon cages or external doping of metal ions has been attempted to gain fullerene-based metal coordination complexes.[15] To date, such two strategies have been successfully developed to fabricate endohedral metallofullerenes and exohedral metallofullerene complexes.[15] Numerous dedicated and detailed studies have discovered that metals and nitride-, oxide-, cyano-, and sulfide-metal clusters were encapsulated inside fullerene cages to obtain conventional metallofullerenes and metal-containing cluster fullerenes.[16] In most cases for investigating the electronic and molecular structure of endohedral metallofullerenes, metal-cage bonding interactions were revealed as the coordination of metal cations with the cage ligand after an appropriate number of valence electrons have transferred to the fullerene cage.[16] Paramagnetic Gd@C_{82}, Gd@C_{60}, Gd_3N@C_{80}, $ScGd_2N$@C_{80}, and Sc_2GdN@C_{80} as representative endohedral metallofullerenes can be used to develop some water-soluble derivatives *via* exohedral and functional modification onto the surface of metallofullerene cages as contrast agents for drastically improving the image quality of

[a]*NanoAgro Center, College of Plant Protection, Henan Agricultural University, Zhengzhou 450046, China. E-mail: wuqingnan@henau.edu.cn*

[b]*National Key Laboratory of Wheat and Maize Crop Science, College of Life Science, Henan Agricultural University, Zhengzhou 450046, China. E-mail: taifuju@henau.edu.cn*

† Electronic supplementary information (ESI) available. See DOI: https://doi.org/10.1039/d3ra07725j

‡ R. H. and C. F. contributed equally to this work.

magnetic resonance imaging (MRI) diagnostic examination and potential application in the biomedical field.[16] However, the yields of endohedral metallofullerenes were extremely low, equivalent to the order of 1% of the empty fullerenes.[16] More researchers focused on exohedral metal–fullerene coordination complexes, including metals directly coordinating to the carbon cage, functionalized fullerene–metal ion coordination complexes, and conjugations of fullerene adducts with metal chelates.[15] Among them, significant progress was achieved in the synthetic procedures and structural studies of metallic complexes with appendant groups of functionalized fullerenes as ligands. According to classification by the hydrophilic or hydrophobic polarities of appended substitutes, functionalized fullerenes are mainly divided into water-insoluble/soluble fullerene adducts. The early discoveries that triggered the interest of scientists were representative hydrophobic fullerene adducts chelating metal ions in nonaqueous solutions, among which bipyridine, terpyridine, pyrazine, and dipyrrolidine were functionalized to fullerenes.[17] In 1998, a dimeric fullerene–Pt coordination complex was firstly reported, where $Pt(Et_3)_2(OTf)_2$ mediated the self-assembly of dipyridylmethanofullerene to form a discrete coordination structure.[18] To take a step forward, a variety of one-, two-, and three-dimensional framework structures were successfully developed, wherein various hydrophobic fullerene adduct ligands chelated with different metal ions in nonaqueous solutions to form diverse metal–fullerene frameworks for providing nanoscale porous spaces.[19–22]

On the other hand, hydrophilic fullerene adducts as the water-soluble derivatives of functionalized fullerenes (*i.e.*, fullerenol is a typical representative) have been widely studied to disclose excellent bioactivities for potential biomedical applications, such as antitumor, antiviral, antibacterial, and antioxidative abilities, and efforts toward building metal-coordinated complexes in aqueous solutions and subsequent application in biomedicine are rather limited.[23,24] In particular, fullerenols have a beneficial π-electron structure and numerous oxygen-containing groups for forming coordinate bonds; thus, their application to fabricate metal-coordinated complexes is eagerly anticipated.[24] Some investigations mentioned the salting out of fullerenols in the cosaturated fullerenol–salt–water ternary systems in the presence of varied inorganic salts to result in precipitates of fullerenols.[25–29] However, the roles of salts were largely unclear on whether metal ions-induced the further assembly of fullerenols *via* coordination or not. The first direct evidence about metal ions coordinating to fullerenols was revealed by Anderson *et al.*, where fullerenols acted as a ligand analogous to a 1,2-diol or catechol to possibly form tetrahedral and octahedral coordination under the stoichiometric condition of fullerenols to metal ions excess of 1 : 10.[30] Hereafter, more researchers demonstrated that the fullerenol–metal ion interactions could lead to corresponding coordination complexes. Recently, it was also clarified that fullerenols underwent self-assembly and acted as tridentate ligands to bind trivalent metal ions with 1,3,5-cyclohexanetriol coordination to be potentially utilized for co-precipitation in the removal of metal ions from contaminated water.[31] As a way forward, fullerenol was grafted on the surface of graphene oxide to strengthen its adsorption capacity and selectivity for accurately and strongly chelating Pb^{2+} *via* the oxygen-containing groups of fullerenols.[6] This strategy may be exploited to develop a potential method for the highly efficient removal and ultra-sensitive determination of Pb^{2+} in complex-matrix samples. Moreover, fullerenol/Ni^{2+} porous composite films were synthesized by fullerenols *via* Ni^{2+} coordination under the hard template of polystyrene microspheres and then embedding in poly(methyl methacrylate) in water. The hybrids displayed efficient nonlinear optical properties through metal–ligand charge transfer to increase electron delocalization. In a similar and earlier study, it was firstly reported that fullerenol/Fe^{3+} microcapsules were produced through coordination between the hydroxyl onto fullerenol cage with Fe^{3+} released from a rusty nail using polystyrene microspheres as templates.[24] The magnetic fullerenol/Fe^{3+} microcapsules had good biocompatibility and colloidal stability in water and serum to exhibit effective antioxidant activities for improving the living environment of cells by scavenging the hydroxyl radical. To the best of our knowledge, fullerenols are the most compatible fullerene-based ligand species for the coordination of multivalent metal ions in aqueous media observed so far. Although various metal ions have been explored following coordination techniques to obtain fullerenol–metal ion-chelated complexes, including Ni^{2+},[32] Pb^{2+},[6] Fe^{3+},[24] as well as Zn^{2+}, Cu^{2+}, Co^{2+}, Cd^{2+}, Ca^{2+}, Mn^{2+}, Ag^{+}, La^{3+}, Nd^{3+}, and Al^{3+},[30,31] an unsolved issue is the unavoidable formation of insoluble and random cross-linking hybrids, making it difficult to obtain water–soluble metal cation–fullerenol complexes for biomedical application. Recently, the fullerenol/Fe^{2+} nanocomposite was developed in aqueous media by simply mixing fullerenol (334 μM) and Fe^{2+} (0.556 μM) in the stoichiometric ratio of 590 : 1.[33] Fe^{2+} did not disturb the further assembly process of fullerenol without a noticeable change in the morphology for the nanocomposite, but its zeta potential was indeed shifted to a more positive value. Importantly, such a nanocomposite exhibited a potentially protective effect on healthy tissues and diminished doxorubicin-induced toxic effects on liver and heart tissues. Another interesting observation was about the interaction of anionic fullerene derivatives and Hg^{2+} ions.[34] Stoichiometric (1 : 1 by moles) amounts of Hg^{2+} was adsorbed by the water-soluble fullerene adduct, $C_{60}(S(CH_2)_{10}CO_2K)_5$ to form hybrid metal–fullerene complexes with aggregation as stable colloidal suspensions in aqueous solution, and it was confirmed that the antidote effect to weaken the bioavailability of Hg^{2+} for *Escherichia coli* cells was comparable with that of Unithiol. In addition, various metal salts as a building block possibly fabricate the diversely structural metal ion–fullerenol complexes by tuning the coordination mode of metal ions on fullerenols, which still receives less attention.[17]

Based on the above studies, one proposed method for addressing the challenge to mitigate the formation of the insoluble complexes is the modulation of the random-crosslinking degree by selecting and strictly controlling the stoichiometric ratios of fullerenols to various metal ions that is tailored to the coordination requirements of water-soluble metal cation–fullerenol complexes with a variety of

possibilities in the directed-assembly mode and to discriminate against insoluble hybrids. Herein, we prepared fullerenol in the anion form by improved alkaline-oxidation approach, and the visual observations were carried out for electrostatic- and coordination-directed further assembly of anionic fullerenol in various salt solutions for producing water-soluble/insoluble metal cation-fullerenol coordination complexes. Furthermore, the optimized condition of feed ratios for the preparation of diverse and water-soluble complexes were quantitative investigated by spectroscopic measurements. The resultant water-soluble metal cation–fullerenol complexes were characterized to comparatively analyze their optical, thermal, electron, and photoelectron properties and directed-assembled morphologies. Our work will not only explore the various directed assembly behavior of fullerenols but also to provide an opportunity to discover water-soluble metal cation-fullerenol coordination complexes as novel carbon structures with desirable properties for potential applications in biomedicine.

2 Experiment section

2.1 Materials

All chemicals, unless otherwise stated, were purchased from commercial sources and used without further purification. C_{60} (purity > 99.9%) was purchased from Henan Puyang Yongxin Reagents Company (China). Quaternary ammonium iminofullerene was prepared according to the experimental method given in recent reports, where the average formula was $C_{60}(NCH_2CH_2NH_3^+{}^{\bullet}CF_3COO^-)_4\cdot 10H_2O$ (refers to **IFQA** hereafter) with molecular weight (MW) of 1588 g mol^{-1}.[35] The other reagents were at least analytical grade.

2.2 Synthesis of negatively charged fullerenol

Fullerenol in anion form (Na^+–fullerenol) was prepared using a modified literature procedure.[36–38] Briefly, 300 mL 0.5 g mL NaOH solution was mixed with 10 mL 40% tetra-*n*-butylammonium hydroxide and 600 mL o-dichlorobenzene solution containing 25 g C_{60} in a 2000 mL volume of flask to be vigorously stirred by a mechanical agitator at 60–70 °C for 5 days. After stopping heating and adding 600 mL deionized water, the mixture was continued to be stirred for 1–2 days, then filtrated, washed with deionized water, and separated. The resulting aqueous solution was evaporated, washed with methanol several times, and redissolved in deionized water, followed by dialysis and drying. The purified powder was marked as **FoI**, and later identified as $C_{60}(OH)_{22}(ONa)_3\cdot 7H_2O$.

2.3 Sample pretreatment of fullerene–salt–water ternary systems

FoI (4.0 mM) and **IFQA** (0.4 mM) stock solutions were prepared in volumetric flasks by dissolving purified powders in deionized water. To prepare the stock solutions of the salts, chlorides of alkali (LiCl, NaCl, and KCl), alkaline earth ($MgCl_2$, $CaCl_2$, and $SrCl_2$), mercury ($HgCl_2$), aluminum ($AlCl_3$), and lanthanum ($LaCl_3$) and sodium salts of acetate (CH_3COONa), carbonate (Na_2CO_3), and sulfate (Na_2SO_4) were dissolved in deionized water in volumetric flasks. For the fullerene–salt–water ternary systems, the concentration of **FoI**/**IFQA** always remained constant while the molar concentration ratios of **FoI**/**IFQA** with respect to the salts varied between 1 : 1000 and 1 : 0. To investigate the salting-out effect of **FoI** in alkali metal salt, acidic, or basic solutions, **FoI** (4.0 mM, 0.5 mL) were diluted upon the addition a series of varying concentrations of KCl, NaCl, LiCl, HCl, Na_2SO_4, Na_2CO_3, CH_3COONa, NaOH, and water (0.5 mL) in plastic centrifuge tubes, where the ratios of **FoI** to them were 1 : 1000, 1 : 500, 1 : 250, 1 : 100, and 1 : 0. To investigate the directed assembly of **FoI** in metal chloride solutions, **FoI** (0.4 mM, 1.0 mL) were diluted twice upon the addition of various concentrations of NaCl (1 : 1000, 1 : 500, 1 : 250, 1 : 100, 1 : 10, and 1 : 0), $MgCl_2$ (1 : 100, 1 : 10, 1 : 7.3, 1 : 6, 1 : 1, and 1 : 0), $AlCl_3$ (1 : 10, 1 : 5, 1 : 2, 1 : 1.6, 1 : 1, and 1 : 0), $LaCl_3$ (1 : 10, 1 : 5, 1 : 1.8, 1 : 1.4, 1 : 1, and 1 : 0), KCl (1 : 1000, 1 : 500, 1 : 250, 1 : 100, 1 : 10, and 1 : 0), $CaCl_2$ (1 : 50, 1 : 5, 1 : 3.8, 1 : 2, 1 : 1, and 1 : 0), $SrCl_2$ (1 : 10, 1 : 5, 1 : 4, 1 : 3.5, 1 : 2, and 1 : 0), and $HgCl_2$ (1 : 1000, 1 : 200, 1 : 100, 1 : 50, 1 : 10, and 1 : 0) in the screw bottles. To investigate the surface charge effect of the fullerene ligand on the directed assembly of metal ion–fullerene hybrids, **IFQA** (0.4 mM, 0.5 mL) were diluted upon the addition of a series of varying concentrations of NaCl, $MgCl_2$, $AlCl_3$, $LaCl_3$, KCl, $CaCl_2$, $SrCl_2$, and $HgCl_2$ (1 : 1000, 1 : 500, 1 : 250, 1 : 100, and 1 : 0, 0.5 mL) in plastic centrifuge tubes. After $HgCl_2$ solution was preblended with a 10-fold equimolar amount of NaCl, 0.5 mL of the resulting solution and **IFQA** (0.4 mM, 0.5 mL, **IFQA** : $HgCl_2$, 1 : 20) were successively added into a plastic centrifuge tube, followed by thorough mixing.

2.4 Visualized observation for the directed assembly/salting-out effect of FoI in salt solutions

Freshly prepared **FoI** with alkali metal salt, acidic, or basic solutions in plastic centrifuge tubes were immediately observed and photographed after centrifugation with 10 000*g* at 4 °C for 5–10 min, whether there was a decoloration of the supernatant and/or some solid at the bottom or not. **FoI** with metal chloride solutions in screw bottles were observed and photographed after standing for 7 days. The freshly prepared **IFQA** with metal chloride solutions were immediately observed and photographed after centrifugation. The concentration ratios that produced precipitates/sediments were recorded.

2.5 Quantitative analysis for the directed assembly of FoI by metal ions

After the treatments in Section 2.4 by ultrasound and centrifugation, the UV-visible spectra of the 5-fold diluted supernatants were measured to record the absorption value at 350 nm. All data analysis was carried out using the three-parameter single exponential growth function as eqn (1).

$$y = A_0 \times \exp(-x/R_0) + y_0 \quad (1)$$

where x corresponds to the **FoI** : metal chloride ratio, y is the remaining absorption value for ternary systems in comparison to metal chlorides, and R_0 and y_0 are the initial concentration

ratio and absorption value for ternary systems in supernatants relative to corresponding metal chlorides. The critical concentration ratio was denoted as R_{50} with 50% reduction of the UV absorption value of ternary systems in comparison to the corresponding metal chlorides. Correspondingly, the c_{50} value of metal chlorides for ternary **Fol**–salt–water systems is defined as the critical concentration of metal chlorides at the ratio of R_{50}. From the exponential fitting curves, the inflection points from the exponential growth interval to plateau interval were deduced as R_t, which provided the indication as the turning points of the concentration ratios to discriminate the formation of insoluble hybrids from water-soluble complexes.

2.6 Fabrication of water-soluble M^{n+}@Fol coordination complexes

In a general procedure, a 200 mL and specific concentration of MCl_n (Mg^{2+}: 2.0 mM, Ca^{2+}: 0.92 mM, Sr^{2+}: 0.4 mM, La^{3+}: 0.34 mM, or Al^{3+}: 0.38 mM) solution was added dropwise into **Fol** (200 mL, 0.4 mM), and subsequently the mixture was allowed to be stirred for 30–60 min at room temperature. After filtration, the resulting filtrate was dialyzed against deionized water using a membrane with molecular weight cutoff of 3500 Da for the removal of free metal salts to harvest the purified water-soluble Mg^{2+}@**Fol**, Ca^{2+}@**Fol**, Sr^{2+}@**Fol**, Al^{3+}@**Fol**, and La^{3+}@**Fol** coordination complexes.

2.7 Characterization

The absorbances at 350 nm and the UV-visible spectra were recorded on an A560 spectrophotometer (AOE Instruments, China). Fourier transform infrared (FTIR) spectroscopy measurements were performed on a Thermo Scientific Nicolet iN10 MX spectrometer (Madison, USA). X-ray photoelectron spectroscopy (XPS) data were obtained by a Thermo Scientific ESCALAB 250Xi spectrometer (Thermo Scientific, USA), with Al Kα X-rays as the excitation source, working voltage of 12.5 kV, and filament current of 16 mA to perform 10 cycles of signal accumulation. Thermogravimetric analysis (TGA) was performed on a PerkinElmer STA 6000 Thermogravimetric Analyzer (TA Instruments, USA) at a heating rate of 10 °C min^{-1} under nitrogen (N_2) atmosphere in a scanning range from room temperature to 1000 °C. The zeta potentials of the samples (20 mg L^{-1}) in deionized water were measured using a Microtrac Nanotrac wave II particle size and zeta potential analyzer (Microtrac Instruments, USA). X-ray Diffraction (XRD) test was performed on an Ultima IV X-ray diffractometer (Rigaku, Japan) in the scanning range from 5° to 90° and at a scanning rate of 2° min^{-1} with Cu Kα X-rays. Transmission electron microscopy (TEM) investigation included conventional and high-resolution TEM (HRTEM) imaging and selected-area electron diffraction (SAED) to observe the size, shape, dispersity, and microstructure, which were studied on an HRTEM (JEOL JEM-2100Plus, Japan) operated at 200 kV accelerating voltage. One drop of ~1 μM aqueous solution of the samples for TEM examination was deposited on Cu grid-supported carbon films to allow drying at room temperature for ~2 hours.

3 Results and discussion

3.1 Characterization of Na^+-fullerenol

As shown in the full survey spectrum of **Fol** in Fig. 1a, the C_{1s}, O_{1s}, and Na_{1s} peaks were observed, and the atomic ratio of C/Na was about 60 : 2.83. The high-resolution Na_{1s} XPS spectrum at the binding energy of 1071 eV is presented in Fig. 1b to indicate Na^+ coexistence in the tested sample, which should be introduced due to the synthesis process.[36,37] The high-resolution O_{1s} spectrum was fitted to three peaks at 531.3, 532.62, and 536.01 eV, ascribing to hydroxyl (C–OH), epoxy group (C–O–C), and alkoxide anion moiety (C–O–/C–O–Na).[6,31] In the FTIR spectrum (Fig. 1d), the appendant –OH and remaining π-bonded carbons of the fullerene cages were validated as the diagnostic criteria for fullerenols with the four characteristic peaks at about 3415, 1585, 1045, and 1385 cm^{-1} assigned to ν_{C-OH}, $\nu_{C=C}$, ν_{O-H}, and δ_{C-OH} adsorptions.[38,39] The thermogravimetric (TG) and differential TG (DTG) curves are shown in Fig. 1e, where the first weight loss (~9.5%) occurred before 136 °C, which was ascribed to bound water. The second-step decomposition (~36.5%) was assigned to the process of dehydroxylation (C–OH, C–O–C, C–O–) of **Fol** between 136 °C and 619 °C. Taking into account that the molecule cannot be fractioned and the results of combination XPS and TGA, the average molecular formula for **Fol** was described as $C_{60}(OH)_{22}(ONa)_3 \cdot 7H_2O$ (MW = 1337 g mol^{-1}).[38] The XRD pattern was a broad diffraction peak at $2\theta = 22.765°$ and is displayed in Fig. 1f (JCPDS 50-0926), indicating an amorphous structure of **Fol** at the macroscopic level.[24,32]

3.2 Salting-out effect of Fol in alkali salt solution

The solubility of **Fol** in aqueous solution of various alkali-metal salts/acid/base was studied by means of room temperature in plastic centrifuge tubes. We recorded the digital photos (Fig. 2) of all the samples with a fixed concentration of **Fol** but varying concentrations of acid, base, and salts. **Fol** (4.0 mM, 0.5 mL, the molar ratio, $c_{\mathbf{Fol}} : c_{\text{alkali metal ion/hydrogen ion}} = 1:1000, 1:500, 1:250, 1:100$, and $1:0$) were mixed with 0.5 mL alkali metal chlorides (KCl, NaCl, or LiCl), sodium salts (CH_3COONa, Na_2CO_3, or Na_2SO_4), HCl, or NaOH. As follows from Fig. 2a–c, the dark- or light-brown precipitates of **Fol** were observed in the bottom of the tubes after centrifuging the aqueous solution of **Fol** upon the addition of KCl, NaCl, or LiCl. The increase in the precipitation (Fig. S1a–c in the ESI†) and discoloration of dark brown of the supernatants (Fig. 2a–c) indicated the reduction in **Fol** solubility in the presence of alkali chlorides (Fig. S2 in the ESI†), which were dependent upon the increase in the concentration of alkali chlorides, namely, the molar ratio of **Fol** to alkali chlorides. After the addition of other sodium salts, more or less precipitates continued to be observed in **Fol**–salt–water ternary systems (Fig. 2e–g). The dissolution of **Fol** in supernatants containing Na_2CO_3 and Na_2SO_4 had a noticeably smaller reduction than those in the presence of CH_3COONa and NaCl (Fig. S2 in the ESI†). For different counter ions, the higher the anionic charge, the less was the precipitation by Na^+. In addition to alkali metal salts, the similar phenomena likely occurred

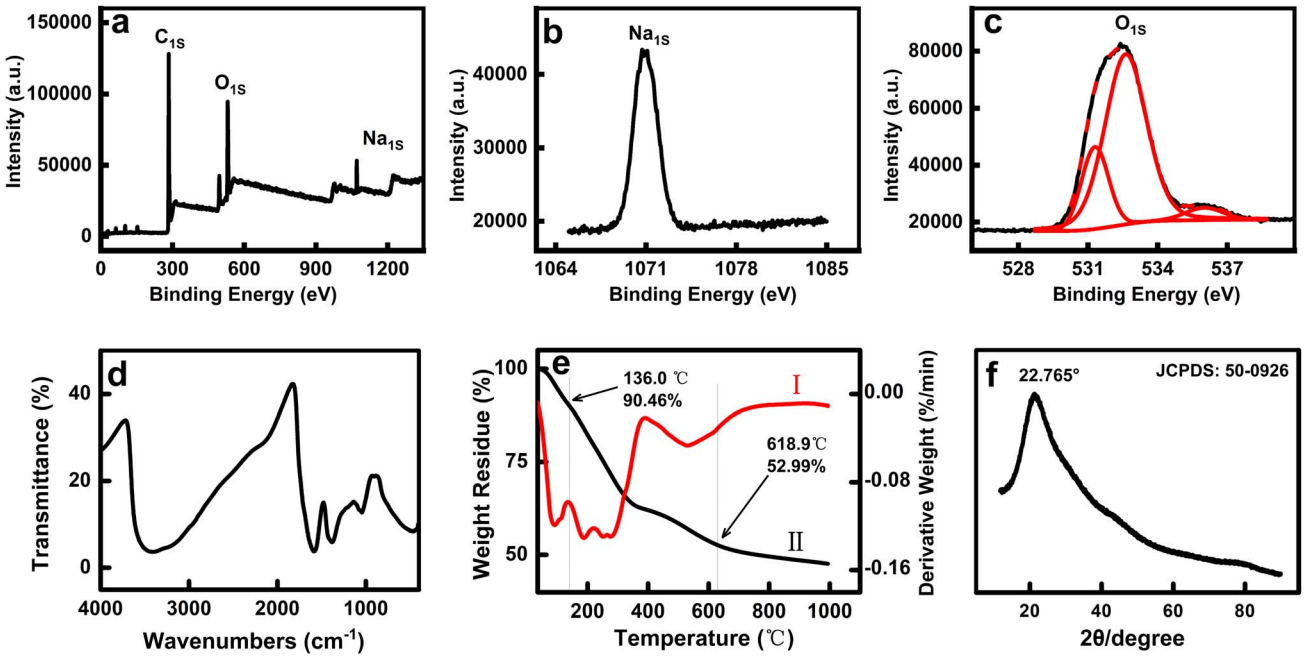

Fig. 1 The full survey (a), high-resolution Na_{1s} (b) and O_{1s} (c) XPS spectra, FTIR spectrum (d), DTG (I) and TG (II) curves (e), and XRD pattern (f) of **Fol**.

in the **Fol**–acid/base–water ternary system (Fig. 2d and h). The higher the concentration of HCl/NaOH, the more the precipitates and decoloration of **Fol** (Fig. S1e and f in the ESI†); correspondingly, the lower the solubility of **Fol** in the supernatant (Fig. S2 in the ESI†).

Furthermore, at 0.8 mM concentration of **Fol**, only a small amount of precipitate was clearly observed in the **Fol**–salt–water ternary systems upon the addition of KCl, NaCl, or CH_3COONa up to a molar ratio of 1 : 1000 (Fig. S3 and S4†). Under the condition of a lower concentration (0.4 mM) of **Fol**, precipitates were no longer produced in ternary systems with arbitrary concentrations of salts (Fig. S5†). Some evidences were demonstrated, where inorganic salts (*i.e.*, NaCl) modulated salting out of fullerenols from saturated fullerenol–salt–water systems.[25,26] On the other hand, in our present study, after decreasing **Fol** solubility in water–**Fol** ternary systems in the presence of alkali metal salts, base, or acid to oversaturate the solution, the supersaturated **Fol** was precipitated. It is worth noting that the above-described and solidified **Fol** (Fig. S1 and S4†) can be thoroughly redissolved in deionized water, and no precipitate will be produced after centrifugation again.

On the whole, we can state with confidence that the salting-out phenomena of **Fol** in the evaluated ternary systems was attributed to the action of alkali metal ions or acid–base regulation. When the concentration of **Fol** is not higher than 0.4 mM and the molar ratio of **Fol** to alkali metal cations is up to 1 : 1000, the **Fol**–alkali metal salt–water ternary systems still maintained dissolution as unsaturated solutions without discoloration and salting out to precipitate **Fol** in the solid state. Also, **Fol** precipitates induced by extremely high concentration

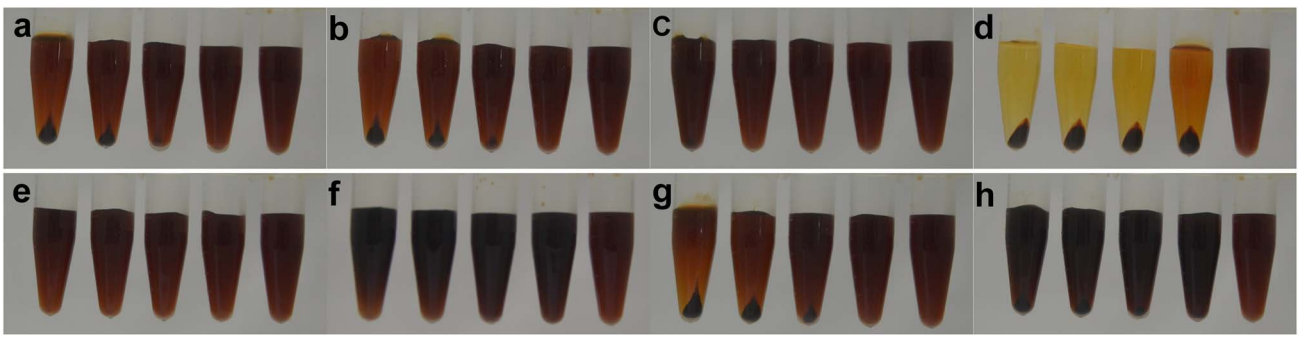

Fig. 2 The photographs of aqueous solutions of **Fol** (4.0 mM, 0.5 mL) upon the addition of equivalent volume of (a) KCl, (b) NaCl, (c) LiCl, (d) HCl, (e) Na_2SO_4, (f) Na_2CO_3, (g) CH_3COONa, or (h) NaOH (from left to right $c_{Fol} : c_{M^+/H^+} = 1 : 1000, 1 : 500, 1 : 250, 1 : 100$, and 1 : 0) in plastic centrifuge tubes after centrifugation. *c* is the molarity of alkali metal ion, hydrogen ion, or **Fol**. The discoloration of the dark brown supernatants indicated the reductions of **Fol** solubility in the presence of alkali chlorides, acid, and base.

of alkali metal cations will be soluble again in water, that is to say, alkali metal cations cannot cause **Fol** to form insoluble aggregates in water.

3.3 Directed assembly of Fol by the coordination effect

The varied metal chloride-mediated further assembly of **Fol** in aqueous solutions was studied by means of room temperature in screw bottles. Since metal cations are more strongly bound to smaller anionic counter ions to reduce the availability of attachment sites to derivatized fullerenes by static-electric force,[40] we selected the salts of multivalent-state metal cations with chloride ion as counter ions, alkaline earth chlorides ($MgCl_2$, $CaCl_2$, and $SrCl_2$), aluminum chloride ($AlCl_3$), transition metallic chloride ($HgCl_2$), and rare earth chloride ($LaCl_3$) to investigate whether and how they affect the further assembly or dissolution of **Fol** in **Fol**-metallic chloride-water ternary systems relative to those of monovalent-state alkali metal chlorides. As shown in Fig. 3a and e, not surprisingly, under the condition of **Fol** (0.2 mM) to NaCl/KCl ratio up to 1 : 1000, the **Fol**–NaCl/KCl–water ternary systems were still unsaturated without sediments after standing for 7 days; on the other hand, the onset of sediment formation in **Fol**–$LaCl_3$–water ternary system was at an extremely low **Fol** : $LaCl_3$ ratio of only 1 : 1.4. **Fol** can be completely sedimented after the 10-fold-equivalent addition of $LaCl_3$ with almost colorless supernatant (Fig. 3d and S6d†). Keskinov *et al.* explained the very strong salting-out effect in fullerenol–D-$LaCl_3$–H_2O ternary system at very low concentrations of fullerenols near eutonic points, where rare earth salt served as a highly-effective salting-out agent.[27,28] Nevertheless, their results did not clarify whether the sediment could be further re-dissolved in deionized water. In our case, it is incomprehensible that the dissolution of the sediment from $LaCl_3$ cannot be observed in 2 mL deionized water in comparison to treatments in Fig. 2, and it fell out of solution and precipitated in the bottom of the tubes after centrifugation again. If the so-called sediment was caused by the salting-out effect, "free" **Fol** can be redissolved in water. Thus, the resulting sediment from $LaCl_3$ should not be due to the salting out effect but is attributed to the coordination effect that allows **Fol**–chelating La^{3+} as a water-insoluble hybrid, which is consistent with the findings of Heimann *et al.*[31] As expected, it was further investigated and found that similar sedimentation events began to be formed in ternary systems in the individual presence of $AlCl_3$, $SrCl_2$, $CaCl_2$, and $MgCl_2$ with the relatively lower molar ratios (**Fol** : metal ion) of 1 : 1.6, 1 : 3.5, 1 : 3.8, and 1 : 7.3 in comparison to those of alkali metal chlorides (Fig. 3b, c, f, and h). When the ratios of **Fol** to $MgCl_2$, $CaCl_2$, $SrCl_2$, and $AlCl_3$ reached 1 : 100, 1 : 50, 1 : 10, and 1 : 10, **Fol** were completely sedimented (Fig. S6b, c and S6f, h†). In addition, the case under treatment of $HgCl_2$ was somewhat unexpected, where the ratios for initial and complete sedimentation were about 1 : 100 and 1 : 1000.

To top it all off, all the sediments/precipitates exhibited in Fig. 3 and S6† cannot be redissolved in deionized water so that they still maintained insoluble capacities after aqueous dispersion–centrifugation process. How to reasonably clarify this phenomenon? Obviously, these sediments/precipitates were not "free" **Fol** but should be the salt–**Fol** composite. Anderson and co-workers elaborated the insoluble complexes by the irreversible reaction of hydroxyfullerene with metal salts.[30,31] They were insoluble random-cross-linked polymers with the lack of an ordered structure, but there were even more metal–fullerenol complexes, where the hydroxylated sidewalls of carbon cages of fullerenols acted as the ligands. Li *et al.* noted a fullerenol-based porous organic–inorganic-hybrid composite film that mixed fullerenols with nickel chloride and polystyrene microsphere solution *via* metal coordination to embed in poly(methyl methacrylate).[32] Our results are consistent with these previous researches. We give a plausible speculation as follows. Under treatments with alkali metal ions only at very high concentrations, salting out occurred to form re-soluble precipitate of **Fol**, which was mainly attributed to the lack of coordination activity of alkali metal cations; hence, they cannot coordinate with **Fol** as alkali metal cation–**Fol** hybrids. However, in stark contrast to the case of NaCl and KCl, treatments with $LaCl_3$, $AlCl_3$, $SrCl_2$, $CaCl_2$, and $MgCl_2$ at an extremely low concentration did cause **Fol** to produce water-insoluble sediment, which was largely dependent on further directed-aggregation due to strong coordination interaction between **Fol** and multivalent metal cations. The monovalent alkali metal salts can only produce the solid-state **Fol** by means of the salting out effect at a relative high concentration ratio (>1 : 100), whereas multivalent metal chlorides can induce **Fol** to form water-insoluble hybrids by means of coordination at the lower concentration ratio (<1 : 10). These findings clearly underline

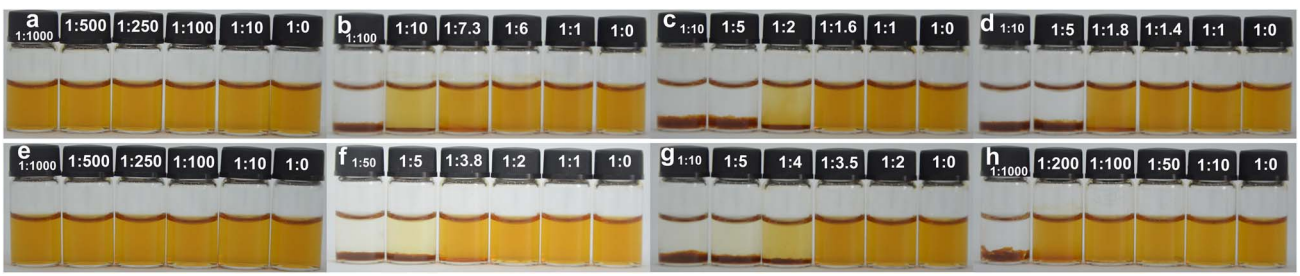

Fig. 3 The photographs of aqueous solutions of **Fol** (0.4 mM, 1.0 mL) upon the addition of varied concentrations (1 : 1000–1 : 0) and equivalent volume of (a) NaCl, (b) $MgCl_2$, (c) $AlCl_3$, (d) $LaCl_3$, (e) KCl, (f) $CaCl_2$, (g) $SrCl_2$, and (h) $HgCl_2$ in the screw bottles after standing for 7 days. The proportion is the molar ratio of **Fol** to metal ion.

that the most important factor for sedimenting **Fol** out of the solution is related to the intrinsic metal cation affinities of coordination to fullerenols rather than to their concentrations. Indeed, coordination strongly influenced the binding activities of metal ions to fullerenols.

3.4 Surface charge of fullerene ligand modulating chelation of metal ions

Besides the coordination effect, another important parameter that strongly influenced the directed assembly of fullerene ligands can be defined as the cage property factor. Thus, the surface charge of the carbon cage also played an important role for metal ions to induce the further assembly of fullerene ligands.

As a new example, we recently synthesized water-soluble and cationic iminofullerene nanoparticles with the terminal amino groups in carbon chains (refers to **IFQA**) to provide the potential coordination binding sites.[35] Under the condition of fixed concentration (0.2 mM) of **IFQA**, not only did the **IFQA**–NaCl/KCl–water ternary systems not produce precipitate (Fig. 4a and e) but also no precipitate was formed in every trial when a series of concentrations of $MgCl_2$, $CaCl_2$, $SrCl_2$, $AlCl_3$, and $LaCl_3$ were individually added into the **IFQA** solution (Fig. 4b–d, f, and g). This implies that there was no coordination interaction between **IFQA** and these metal chlorides. An interesting phenomenon was also observed at a higher concentration (2.0 mM) of **IFQA**, where the ternary systems still did not produce precipitate after the addition of these chlorides up to 1000-fold equivalent amount (Fig. S7b–h†). This is reminiscent of the strikingly different behavior of **Fol**-induced sedimentation in the presence of the above-mentioned metal chlorides, where similar effects can be discounted for the present example on the basis that the sediment could be achieved in binding experiments of metal cations and **Fol** in Fig. 3. The surface charge properties of fullerene ligand strongly affect the metal cation attachment by affecting the static-electric force, which forms metal cation–fullerene coordination complex.[40] Cationic **IFQA** can prevent the adsorption of metal cations due to the repulsive coulombic force and consequently cannot cause the coordination action.[41] On the other hand, **Fol** has a negative zeta potential (Table 2) that readily exists as polyanion aggregates.[36] The anionic **Fol** allowed multivalent metal cations to be easily absorbed onto the surface of carbon cages, resulting in coordination with polyhydroxyl groups on cages to subsequently form metal cation–**Fol** hybrids.[31] **Fol**, as the electronegative fullerene ligand on the attachment of metallic cations, were mainly controlled by electrostatic attraction forces; on the contrary, **IFQA**, as an electropositive ligand, repelled the attachment of metallic cations and then prevented the formation of metal cation and **IFQA** complex.

There was an apparent exception to the general correlation in the observation of electrostatic repulsion between metal cations and **IFQA**, where precipitation occurred after adding more than 500-fold equivalent amount of $HgCl_2$ into **IFQA** (Fig. 4h and S7a†). The discoloration of brown **IFQA** and precipitate formation in the presence of $HgCl_2$ indicated that the $HgCl_2$ and **IFQA** complex was unexpectedly generated, *i.e.*, $HgCl_2$ can induce the further assembly of **IFQA** by coordination. Non-fading **IFQA** (Fig. 4a–g) indicated that **IFQA** did not bind metal cations to form insoluble hybrids. $HgCl_2$ as a pseudo salt is a weakly ionized covalent compound that mainly exists in the form of $HgCl_2$ molecules in dilute solution with no more than 3% ionization.[42,43] Only a very small amount of $HgCl_2$ was ionized as $[HgCl]^+$, Hg^{2+}, and Cl^- ions. Since there is electrostatic repulsion between $[HgCl]^+$ and Hg^{2+} with **IFQA**, the resulting complex should be the $HgCl_2$–**IFQA** coordination complex formed by $HgCl_2$ molecules binding directly to **IFQA**. On the other hand, as shown in Fig. S6h,† the $HgCl_2$ and **Fol** complex was relatively easier to generate than the $HgCl_2$–**IFQA** complex (the onset on precipitation, 1 : 100 *vs.* 1 : 500). Even though the ionization of $HgCl_2$ was very low, under $HgCl_2$ and more than 100 equivalents of **Fol**, the concentration of Hg^{2+} ion in the solution was comparable to that of **Fol**, which may result in the formation of Hg^{2+}–**Fol** and/or $[HgCl]^+$–**Fol** complexes by electrostatic attraction and then coordination actions. In these cases, the directed assembly behavior of fullerene derivatives in salt solutions, especially **Fol**, has been observed qualitatively. In the following section, the behavior will be quantificationally investigated.

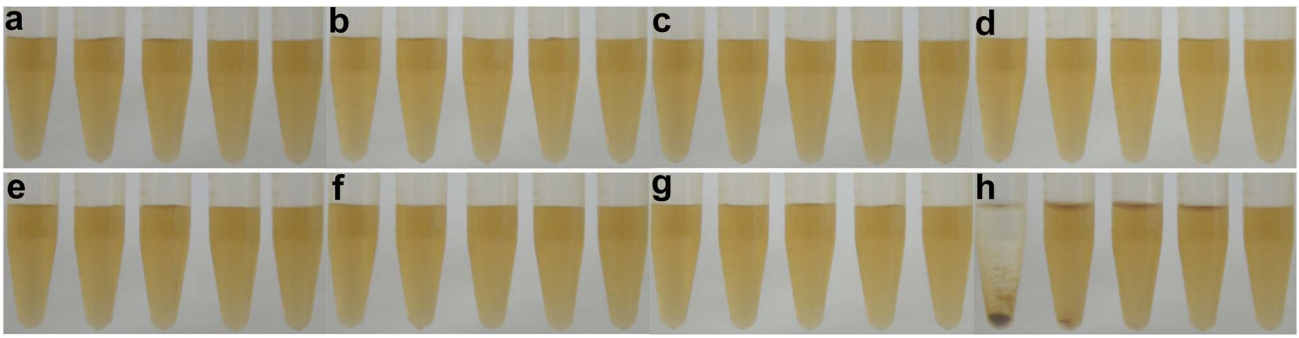

Fig. 4 The photographs of aqueous solutions of IFQA (0.4 mM, 0.5 mL) upon the addition of equivalent volume of (a) NaCl, (b) $MgCl_2$, (c) $AlCl_3$, (d) $LaCl_3$, (e) KCl, (f) $CaCl_2$, (g) $SrCl_2$, and (h) $HgCl_2$ (from left to right $c_{IFQA} : cM^{n+} = 1:1000, 1:500, 1:250, 1:100$, and $1:0$) in plastic centrifuge tubes after centrifugation. c is the molarity of metal ion or IFQA.

3.5 Quantification of inducibility of metal chlorides for directed assembly of FoI

According to the visualization observations in Fig. 3a and e, adding the no matter how high concentration of alkali metal chlorides cannot cause further assembly of **FoI** that it is always impossible to produce insoluble complexes. Nevertheless, multivalent metal chlorides modulate the further assembly of **FoI**, which appeared to be a variation tendency heavily influenced by the type of the metal cations whose ratio for initial formation of sediment was observed approximately at 1 : 1–1 : 10 in Fig. 3.

The typical UV spectral curves of **FoI**–metal chloride–water ternary systems are depicted in Fig. S8,† which seem to be very similar. In all cases, a reduction of the absorbance intensity at 350 nm was associated with the gradually increased addition of metal chlorides with the **FoI** : metal chloride ratio between 1 : 0.5 and 1 : 900, which illustrated that **FoI** can be bound to precipitate and fall out of the solution. In order to precisely evaluate the inducibility of metal cations for directing the assembly of **FoI**, the absorbance value was used to quantify c_{50}. In this manner, the UV-adsorption value was measured to analyze the amount of complexed precipitates and remaining **FoI** in the supernatant. We started with a known amount of **FoI** (0.4 mM, 0.5 mL) and added 0.5 mL varied multivalent metal chlorides with the initial **FoI** : metal chloride ratio of 1 : 0.5, but no precipitate was observed in all the samples. Subsequently, we kept increasing the concentrations of metal chlorides added until all of **FoI** was precipitated.

To validate the R_{50} for various metal chlorides, three-parameter single exponential growth function was proposed as eqn (1) for non-linear curve analysis. The plot shown in Fig. 5d illustrated the correlations of absorption value for the **FoI**–$LaCl_3$–water ternary systems *vs.* $LaCl_3$. It was exponentially recovered from −0.1683 to 0.5957 when $LaCl_3$ was added with the **FoI** : $LaCl_3$ ratio in the range from 1 : 2 to 1 : 0.7, and then reached a peak of 0.6023 at the ratio of 1 : 0.5. It is interesting that the absorption of the **FoI**–$LaCl_3$–water ternary system is negative at the ratio of 1 : 2 in comparison to the $LaCl_3$ solution. It can be seen as a further indication that the anticipated formation of insoluble $LaCl_3$–**FoI** hybrids was accompanied by La^{3+} attachment to **FoI**. This caused initial $LaCl_3$ and **FoI** to fall out of the solution so that the actual absorption value of the ternary system was lower than that of $LaCl_3$ solution alone. By fitting the data to eqn (1), the R_{50} of $LaCl_3$ was deduced to be 0.6462. Taking into account that the concentration of **FoI** was fixed at 0.2 mM, the c_{50} value of La^{3+} was calculated to be 0.3 mM (Table 1), where the average number of bound La^{3+} per **FoI** carbon cage was about 1.6, resulting in precipitation, which downregulated the absorbance by 50%. It revealed that La^{3+} had a high efficacy for inducing the further assembly of **FoI** to produce water-insoluble La^{3+}–**FoI** hybrids. Turning back to Fig. 5, other metal chlorides were also tested in the same manner, and the summary of the details and key data are listed in Table 1. Very similar results were obtained in the case of Al^{3+}, whose R_{50} was 0.5026, close to that of La^{3+}. However, the R_{50} values of alkaline earth metal chlorides were far from the above value at 0.1356 (Sr^{2+}), 0.04737 (Ca^{2+}), and 0.008155 (Mg^{2+}). In addition, the R_{50} of $HgCl_2$ was 0.002030, which was substantially two orders of magnitude lower than that of La^{3+} and Al^{3+}.

The R_{50} quantification can provide a relatively effective strategy to evaluate the inducibility of metal cations/$HgCl_2$ for the directed assembly of **FoI** through electrostatic and/or coordination effects. For the comparison of relatively active effects of metal chlorides on binding **FoI**, we determined that the order of critical concentration was $HgCl_2$ (98.5 mM) ≫ Mg^{2+} (24.5 mM) > Ca^{2+} (4.2 mM) > Sr^{2+} (1.5 mM) > Al^{3+} (0.4 mM) > La^{3+} (0.3 mM) (Table 1). Accordingly, except for $HgCl_2$, the average number of attachment metal cations per **FoI** carbon cage on the surface was about 1.6 (La^{3+}), 2.0 (Al^{3+}), 7.3 (Sr^{2+}), 21.1 (Ca^{2+}), and 122.6 (Mg^{2+}). Thus, the efficiency of induction for **FoI** to further agglomerate into water-insoluble metal cation–**FoI** hybrids is La^{3+} > Al^{3+} > Sr^{2+} > Ca^{2+} > Mg^{2+} ≫ $HgCl_2$. The order of directed assembly of **FoI** follows the charge number of the metal cation as well as its ionic radius.[31] For example, the inductive ability of trivalent cations is always better than those of divalent cations; for divalent cations, the inducibility is stronger for larger cations, same as that for trivalent cations.

3.6 Fabrication and characterization of water-soluble M^{n+}@FoI coordination complexes

Turning back to Fig. 5, for the exponential fitting curves, R_t was validated as shown in Table 1 to be 0.012 ($HgCl_2$), 0.20 (Mg^{2+}), 0.42 (Ca^{2+}), 0.72 (Sr^{2+}), 1.04 (Al^{3+}), and 1.17 (La^{3+}). To the right region of R_t on the curves, the absorption values remained almost constant, which meant that no insoluble hybrids precipitated under the test conditions. The sequence of the R_t value was consistent with the preliminary results of the directly visualized observation in Fig. 3 about the onset ratio of sediment formation. In other words, R_t can be regarded as the starting point for metal cations inducing **FoI** to produce insoluble hybrids and also indicates the inducible ability of various metal cations to drive the further assembly of **FoI**. Since it was validated that **FoI** were coordinated as water-insoluble and disordered microstructures under relatively high concentrations of various metal chlorides, we came up with a reasonable speculation: the complexes will still be formed and exist in ternary solutions, even as a "locally ordered microstructure", at a lower concentration of various metal chlorides with the ratio exceeding R_t. This is also of potential importance where it is desirable to harvest novel water-soluble M^{n+}@**FoI** coordination complexes. In a typical approach for facile fabricating diverse and water-soluble M^{n+}@**FoI** complexes, MCl_n with concentration no more than that for R_t was individually added drop by drop into **FoI** solution at a specific concentration under room temperature. After reaction, the resultant solution was dialyzed to obtain the purified product. Our strategy had considerable merits, such as facile and mild reaction condition, versatility of reaction method, diversity of product, simplicity of after-treatment, and almost no water-insoluble byproduct.

Although the four features in the FTIR spectra of M^{n+}@**FoI** remained constant in comparison to **FoI** (Fig. 6), the complexation between **FoI** and M^{n+} led to clear changes in the IR

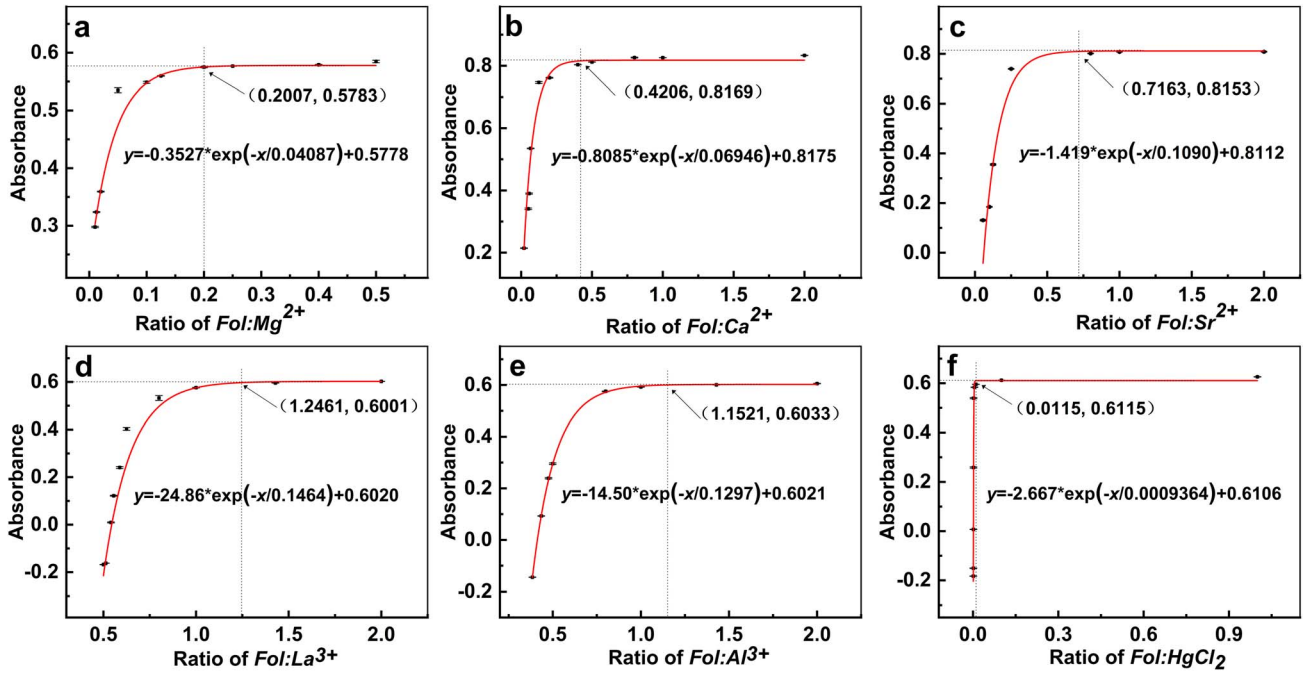

Fig. 5 The exponentially fitting curves of the absorbance recovery of 5-fold diluted supernatants for ternary **Fol**–metal chloride–water systems in comparison to those of the corresponding concentrations of metal chlorides accompanied by an increase in the **Fol** : metal chloride ratio between 1 : 900 and 1 : 0.5. The initial concentration of **Fol** is 0.2 mM. (a) $MgCl_2$, (b) $CaCl_2$, (c) $SrCl_2$, (d) $LaCl_3$, (e) $AlCl_3$, and (f) $HgCl_2$. Data are mean values ± SE for triplicate.

absorption properties. The new and weak absorption peaks were located at 1220–1280 cm^{-1} and assigned to metal and oxygen (M–O) vibration bands (Fig. 6 and Table 2). It is consistent with the phenomena observed for other metal hybrids that the complexation would induce a stronger absorption band for M–O stretching.[32,44,45] Another new peak at about 1710–1720 cm^{-1} implied the existence of oxygenous groups such as carboxylic, carbonyl, and/or hemi-acetal structure (Table 2),[39] which may be caused by the oxidation effect of metal cation catalysis. In addition, C–OH stretching vibration bands were also observed to slightly shift toward high wavenumbers relative to **Fol** (Table 2). The blue shift of C–OH stretching in combination with the observed M–O vibration bands revealed the coordination formation of **Fol** with various metal ions.

XPS investigation was carried out so as to provide valuable insights into elements and their chemical states. From the full survey spectra (Fig. 7(a1)–(e1)), the photoelectron peaks of C (285 eV) and O elements (531 eV) were always observed in M^{n+}@**Fol** complexes, and the corresponding metal elements were individually detected. For example, the high-resolution Mg_{1s} spectrum is presented in Fig. 7(a2) with the Mg_{1s} peak at a binding energy of 1303.85 eV. Furthermore, the peaks of Ca_{2p} (346.98 eV), Sr_{3d} (133.48 eV), La_{2p} (838.08 eV), and Al_{2p} (74.68 eV) are always present in the high-resolution spectra of the corresponding metal for other complexes (Fig. 7(b2)–(e2)). These disclosed that M^{n+} with **Fol** can coexist in the tested

Table 1 Calculation of the critical concentration of metal chlorides for binding **Fol** on the basis of the analysis of the remaining absorbance of **Fol**–metal chloride–water ternary systems in the supernatant corresponded to the **Fol** : metal chloride ratios

Metal chloride	Fitting formula $y = -A_0 \times \exp(-x/R_0) + y_0$	R_{50}	c_{50} (mM)	Average number of attachment metal ions per **Fol** cage	R_t
$LaCl_3$	$y = -24.86 \times \exp(-x/0.1464) + 0.6020$	0.6462	0.3	1.6 : 1	1.1735
$AlCl_3$	$Y = -14.50 \times \exp(-x/0.1297) + 0.6021$	0.5026	0.4	2.0 : 1	1.0401
$SrCl_2$	$y = -1.419 \times \exp(-x/0.1090) + 0.8112$	0.1365	1.5	7.3 : 1	0.7163
$CaCl_2$	$y = -0.8085 \times \exp(-x/0.06946) + 0.8175$	0.04737	4.2	21.1 : 1	0.4206
$MgCl_2$	$y = -0.3527 \times \exp(-x/0.04087) + 0.5578$	0.008155	24.5	122.6 : 1	0.2007
$HgCl_2$	$y = -2.667 \times \exp(-x/0.0009364) + 0.6016$	0.002030	98.5	492.7 : 1[a]	0.0115

[a] The initial concentration of **Fol** is 0.2 mM; R_{50} is the **Fol**: metal chloride ratio for 50% reduction of the UV absorption value of ternary systems in comparison to corresponding metal chlorides; c_{50} is equal to 0.2 mM divided by R_{50}; R_t is the **Fol**: metal chloride ratio for turning points from the exponential growth interval to plateau interval.

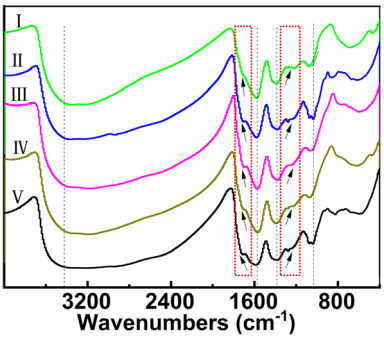

Fig. 6 Comparative FTIR spectra of Mg^{2+}@Fol (I), Ca^{2+}@Fol (II), Sr^{2+}@Fol (III), La^{3+}@Fol (IV), and Al^{3+}@Fol (V).

samples. In addition, it should be noted that the Na_{1s} peaks from the XPS survey spectra of Mg^{2+}@**Fol**, Ca^{2+}@**Fol**, Sr^{2+}@**Fol**, La^{3+}@**Fol**, and Al^{3+}@**Fol** eventually disappeared, as shown in Fig. 7(a1)–(e1). This suggested that divalent and trivalent metal cations had stronger competitive affinity to be adsorbed and coordinate themselves to **Fol** after expelling and consequently replacing the remaining Na^+ in **Fol**. The phenomena had a close similarity with the report on competitively coexisting metal ions with fullerenols to provide an indication of the relative efficacy of metal cations binding fullerenols.[31] The disappearance of the Na_{1s} peak can indirectly indicate whether the investigated metal cations and **Fol** were coordinated to produce the corresponding M^{n+}@**Fol** complexes. The atomic ratio of C/M^{n+} was calculated by XPS to be 60 : 1.40 (Mg^{2+}@**Fol**), 60 : 0.94 (Ca^{2+}@**Fol**), 60 : 0.85 (Sr^{2+}@**Fol**), 60 : 1.05 (La^{3+}@**Fol**), and 60 : 2.32 (Al^{3+}@**Fol**), which revealed the composition in a limited depth for M^{n+}@**Fol** complexes.[32] Among them, the ratios of C/La^{3+} and C/Al^{3+} were higher than those of the corresponding feed concentration ratios, indicating that trivalent La^{3+} and Al^{3+} were more likely to bind and enrich on the surfaces of directed-assemblies after complexation.[32] On the other hand, when Na^+ were replaced by other M^{n+} to form M^{n+}@**Fol** complexes, the high-resolution O_{1s} spectra were fitted into three peaks for different oxidation states (Fig. 7(a3)–(e3)). The positions of C–OH and C–O–C were almost unchanged relative to those of **Fol** (Fig. 1c). However, the metal-oxide anion peaks (C–O–M) were shifted to lower energy region (Fig. 7(a3)–(e3)). It is consistent with the results reported in the previous literature.[31] Thus, the overall XPS results implied that cationic M^{n+} made bonds with polyanionic **Fol** to produce the novel water-soluble M^{n+}@**Fol** coordination complexes.

The TGA curves of M^{n+}@**Fol** also displayed the degradation processes for weight loss of bound water and dehydroxylation similar to those of **Fol**; however, the contents of bound water are always significantly higher than that of **Fol** after complexation (Fig. 8a–e). Moreover, unlike the TG curve of **Fol**, M^{n+}@**Fol** always experienced drastic and continuous decompositions above 600 °C (Fig. 8a–e), which is interpreted in terms of a potential catalytic effect of multivalent metal cations on the degradation of **Fol** carbon cages.[32]

The zeta potential of **Fol** in deionic water was −76.4 mV, while the M^{n+}@**Fol** assemblies displayed positive charge (Table 2). The tested zeta potential changed from negative to positive before and after forming the complexes, providing evidence that cationic M^{n+} were bonded to polyanionic **Fol** aggregates.[33] The crystallinity of M^{n+}@**Fol** complexes was detected by XRD and shown in Fig. 8f, where the halo at 22.765° is the same as that for **Fol** (JCPDS 50-0926), indicating their non-crystallizable macroscopic structures.[24]

3.7 Nanoscale-ordered microstructures of water-soluble M^{n+}@Fol coordination complexes

Besides the optical, thermal, electron, and photoelectron properties, the directed-assembled morphologies of M^{n+}@**Fol** also changed greatly by complexation. As shown in Fig. 9(f1) and (f2), TEM observations displayed nano-sized particle-aggregated microstructure and monomodal and near-ellipsoidal morphology without a smooth surface for the as-synthesized **Fol** sample, which was statistically analyzed to have an average size of 25 nm with distribution in the range of 20–30 nm. After complexation, Mg^{2+}@**Fol** nanoparticles maintained an ellipsoid shape similar to **Fol** with increased average size of 40 nm (Fig. 9(a1) and (a2)), while Ca^{2+}@**Fol** appeared as irregular and uneven nanoparticles with slightly higher average size of 35 nm (Fig. 9(b1) and (b2)). With the complexation of Sr^{2+} to **Fol**, the particle size of Sr^{2+}@**Fol** significantly enlarged to about 60–70 nm, the surface of the nanoparticles gradually became rough, and the shadow in the local area of the TEM image deepened, indicating the successful Sr^{2+}-mediated modification of the **Fol** assembly (Fig. 9(c1) and (c2)). La^{3+}@**Fol** grew as larger assemblies with approximately olive-shaped morphology (Fig. 9(d1) and (d2)), which was different from

Table 2 The key FTIR, XPS, and zeta potential data for M^{n+}@Fol and Fol

	FTIR data			XPS data		Zeta potential
Sample	$\nu_{C=O}$ (cm^{-1})	ν_{M-O} (cm^{-1})	ν_{C-OH} (cm^{-1})	O_{1s} binding energies of fitting C–OH/C–O–C/C–O–M (eV)	The ratio of C/M^{n+}	(mV)
Mg^{2+}@**Fol**	1720	1280, 1220	1070	531.30/532.50/533.46	60 : 1.40	> +200
Ca^{2+}@**Fol**	1710	1280, 1220	1070, 1040	531.30/532.38/533.42	60 : 0.94	+123.2
Sr^{2+}@**Fol**	1710	1230	1070	531.30/532.29/533.52	60 : 0.85	+150.5
La^{3+}@**Fol**	1710	1280, 1220	1080	531.30/532.56/533.54	60 : 1.05	+166.5
Al^{3+}@**Fol**	1720	1280, 1230	1080, 1040	531.30/532.18/533.19	60 : 2.32	+135.7
Fol	—	—	1045	531.30/532.62/536.01	60 : 2.83	−76.4

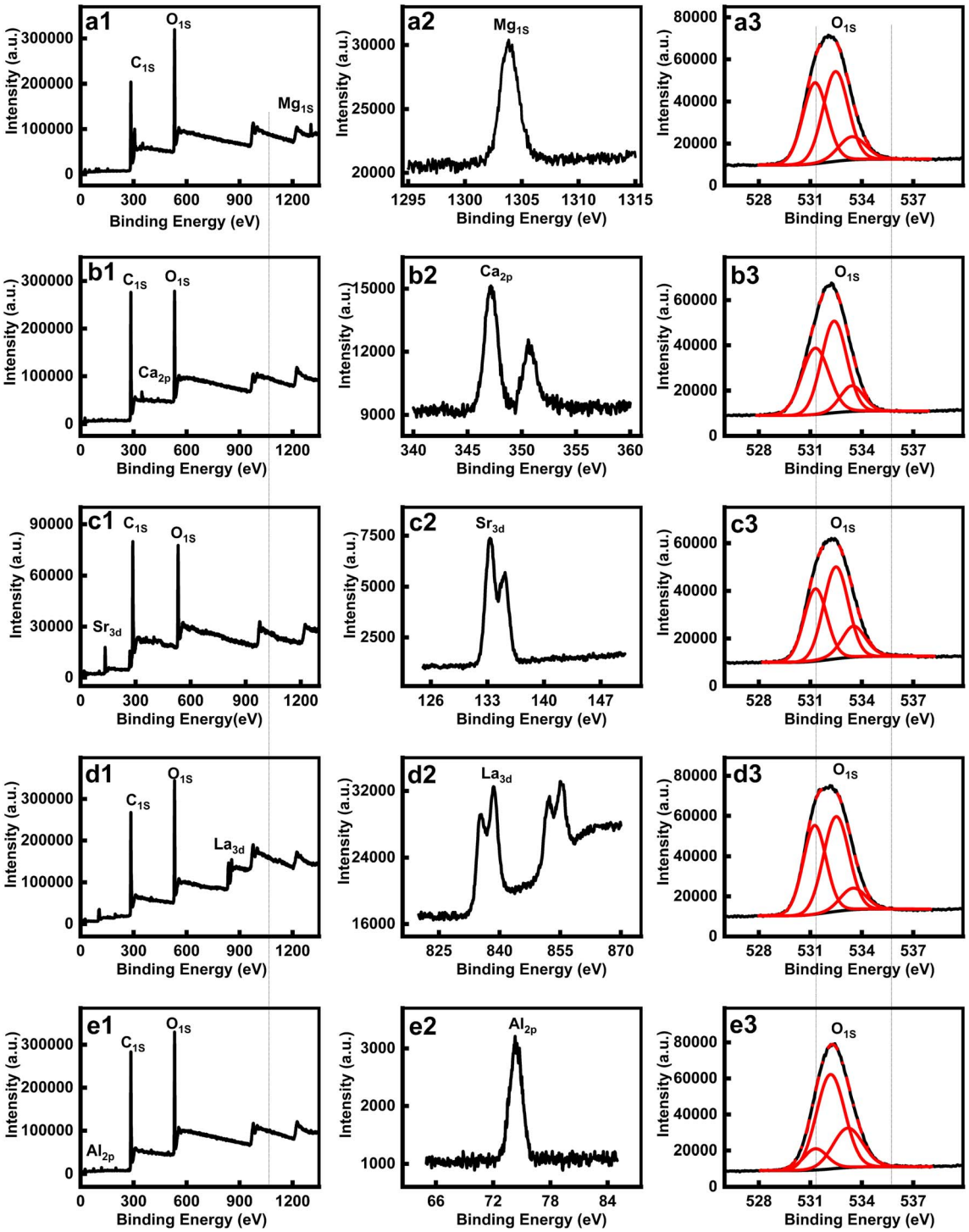

Fig. 7 XPS survey spectra of (a1) Mg^{2+}@**FoI**, (b1) Ca^{2+}@**FoI**, (c1) Sr^{2+}@**FoI**, (d1) La^{3+}@**FoI**, and (e1) Al^{3+}@**FoI**, and their high-resolution XPS spectra of the core level of the corresponding metal ions (a2–e2) and O_{1s} (a3–e3). For O_{1s} spectra, solid black lines are the experimental data, dotted red lines are the deconvoluted spectra, and solid red lines are the fitted oxygen peaks for various oxidation states.

that of the **FoI** and M^{2+}@**FoI** complexes. We described the direction of growth in accordance with the similar one-dimensional rod-like directed-assemblies to display irregular size, up to 65 nm in diameter and up to 270 nm in length. Al^{3+}@**FoI** exhibited the strongest clustering trend as well-dispersed near-spherical nanoparticles with the highest average size of 370 nm (Fig. 9(e1) and (e2)).

Although the crystallinity of M^{n+}@**FoI** complexes was detected by XRD to indicate their amorphous structures, the degree of order in the nanometer length scale and microstructures of these directed-assemblies was further proved by HRTEM. The

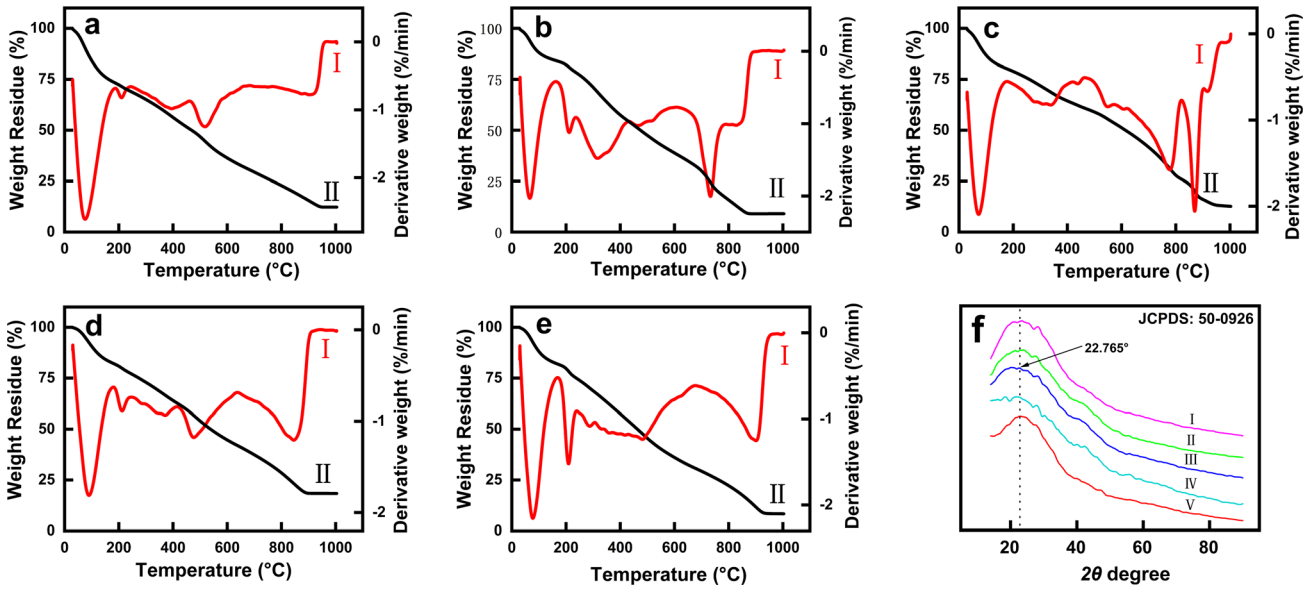

Fig. 8 DTG (I) and TG (II) curves of (a) Mg^{2+}@**FoI**, (b) Ca^{2+}@**FoI**, (c) Sr^{2+}@**FoI**, (d) La^{3+}@**FoI**, (e) Al^{3+}@**FoI**, and (f) XRD patterns for Mg^{2+}@**FoI** (I), Ca^{2+}@**FoI** (II), Sr^{2+}@**FoI** (III), La^{3+}@**FoI** (IV), and Al^{3+}@**FoI** (V).

HRTEM image and SAED pattern of **FoI** showed a typically disordered microstructure without crystallinity (Fig. 9(f3)), which is consistent with the previously reported results.[46] Nevertheless, as shown in Fig. 9(a3)–(d3), some degree of crystallinity is always observed in the HRTEM mode, which indicated the locally ordered microstructures in the nanoscale after complexation. In general, the SAED patterns of M^{n+}@**FoI** complexes displayed a weak spot or ring diffraction patterns (insets of Fig. 9(a3)–(d3)), which can be taken as a further indication of a rather "locally ordered microstructure" formation of the water-soluble M^{n+}@**FoI** complex as nanocrystalline. Mg^{2+}@**FoI** nanoparticles showed a tiny weak signal for a slightly ordered microstructure with almost no morphological changes; Ca^{2+}@**FoI** and Sr^{2+}@**FoI** exhibited locally-ordered microstructures accompanied by slight changes in the morphology and size, while the most ordered nanoscale areas and morphological change from zero to one dimensional aggregate were confirmed in the La^{3+}@**FoI** sample. The observed crystallinity should be owing to the further aggregation of **FoI**, preferentially with metal ions and not themselves.

The exception was the Al^{3+}@**FoI** complex, which produced no diffraction spots or rings, implying that it did not have a nanoscale microstructure. As discussed elsewhere, the insoluble hybrids were observed at relatively high concentration of salts, indicating that random cross-linked complexation resulted in disordered arrangement.[31] In these cases, salt treatments with higher concentrations were usually better for unordered microstructural cross-linkings. The finding achieved by the TEM experiments is in fact the "locally ordered microstructure in nanoscale" approach toward water-soluble M^{n+}@**FoI** formation under chlorides at a lower concentration (*i.e.*, below that of R_t), where the degree of random crosslinking is insufficient. The disordered microstructure of Al^{3+}@**FoI** may be due to its strongest directed assembly tendency to result in higher degree of random crosslinking relative to other M^{n+}@**FoI**.

3.8 Complexation pathway of metal ion-induced aggregation of derivatized fullerenes

The mechanism of complexation of metal-contained ions and water-soluble derivatives of fullerenes consists of two stages: electrostatic attachment and coordination, where the mode of actions are given in Fig. 10. The electrostatic action was evaluated to play a crucial role for generating metal ion–fullerene complexes, where the surface charge of water-soluble fullerene-based ligands is a critical factor for the complexation in solution through the interaction of electrostatic attraction to strongly attract the metal ions onto ligands.[40] Only the negatively-charged fullerene derivatives, especially fullerenols, can attract the bare metal cations to easily form metal cation-fullerenol complexes in water. **FoI** as the polyanion can adsorb various M^{n+} on the surface of carbon cages through electrostatic attraction. The tested zeta potential shifted from negative to positive before and after the attachment of M^{n+} (Table 2), indicating the cationization after interaction M^{n+} and **FoI** (Fig. 10a). Furthermore, cationization caused M^{n+} to approach the oxygen-contained ligands onto the surface of **FoI** cage and consequently to be chelated through coordination to form multidentate M^{n+}@**FoI** complexes, where the formation process was very rapid. As shown in Fig. 10a, under the condition of the **FoI** : M^{n+} ratio more than R_t, the contents of **FoI** in ternary **FoI**–MCl_n–H_2O systems were hardly ever changed, as confirmed by the UV-visible spectra (Fig. 6 and S8†), indicating that the resultant M^{n+}@**FoI** complexes were water-soluble. Under the condition of the **FoI** : M^{n+} ratio no more than R_t with the increase in the metal–cation concentration, the water-soluble M^{n+}@**FoI** complexes were cross-linked through further

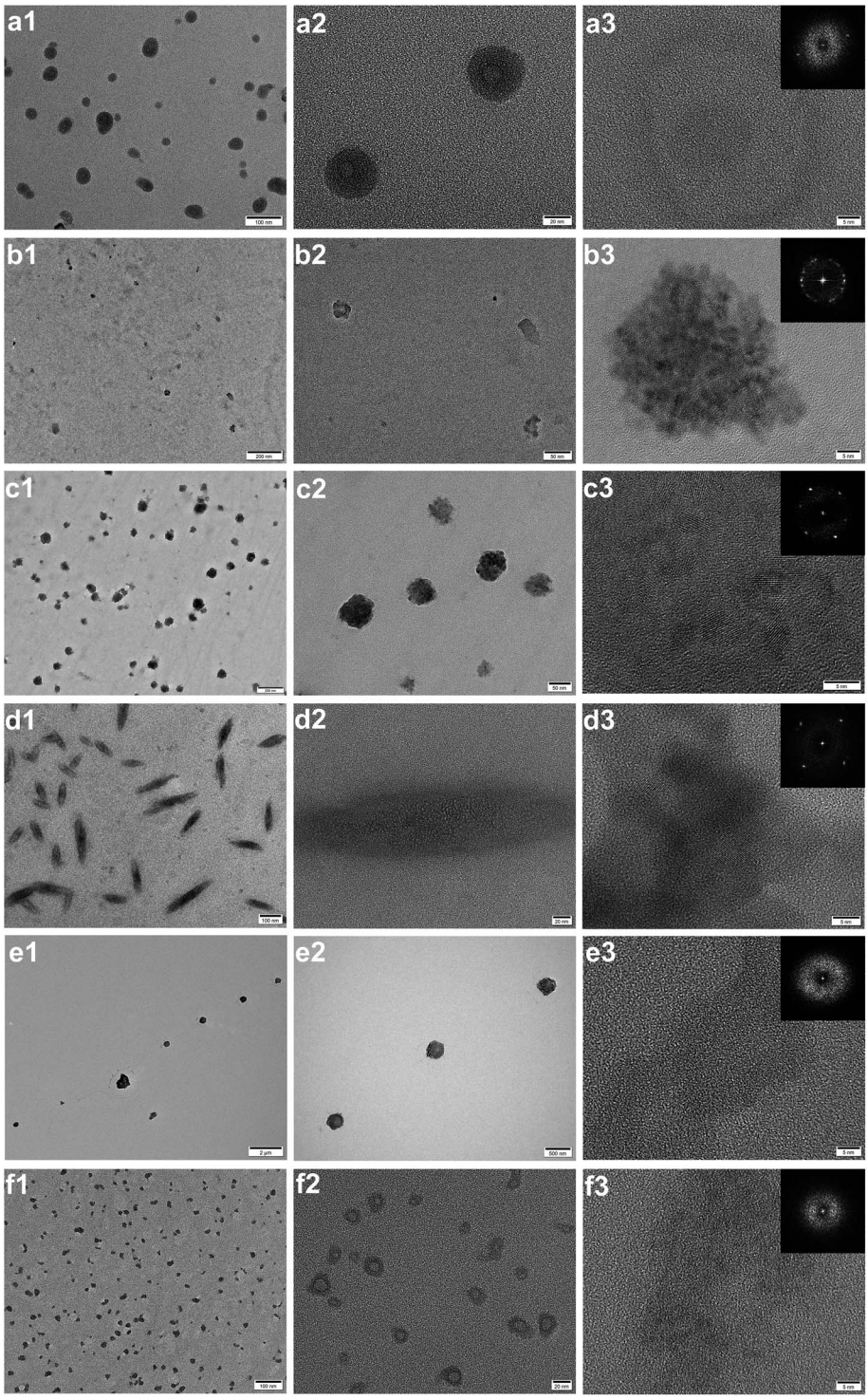

Fig. 9 Comparative TEM (a1–f1, a2–f2) and HRTEM (a3–f3) photos of the directed-assemblies formed by (a) Mg^{2+}@**Fol**, (b) Ca^{2+}@**Fol**, (c) Sr^{2+}@**Fol**, (d) La^{3+}@**Fol**, (e) Al^{3+}@**Fol**, and (f) **Fol** aqueous solution microfilms. Insets in a3–f3 are the microdiffraction patterns.

coordination to larger particles and ultimately the co-precipitation to form insoluble hybrids. Comparing the usage of tri-valent metal cations with di-valent metal cations, the morphology of the resulting water-soluble nanocluster complexes La^{3+}@**Fol** and Al^{3+}@**Fol** had a larger particle size and a more disordered microstructure relative to those of Mg^{2+}@**Fol**, Ca^{2+}@**Fol**, and Sr^{2+}@**Fol** (Fig. 9); meanwhile, the results of the inducibility for the directed assembly of **Fol** also validated the efficiency of tri-valent cations superior to divalent cations (Fig. 5 and Table 2). These implied that higher valent ions were more likely to induce the self-assembly of **Fol** for the formation of complexes with a higher degree of crosslinking *via*

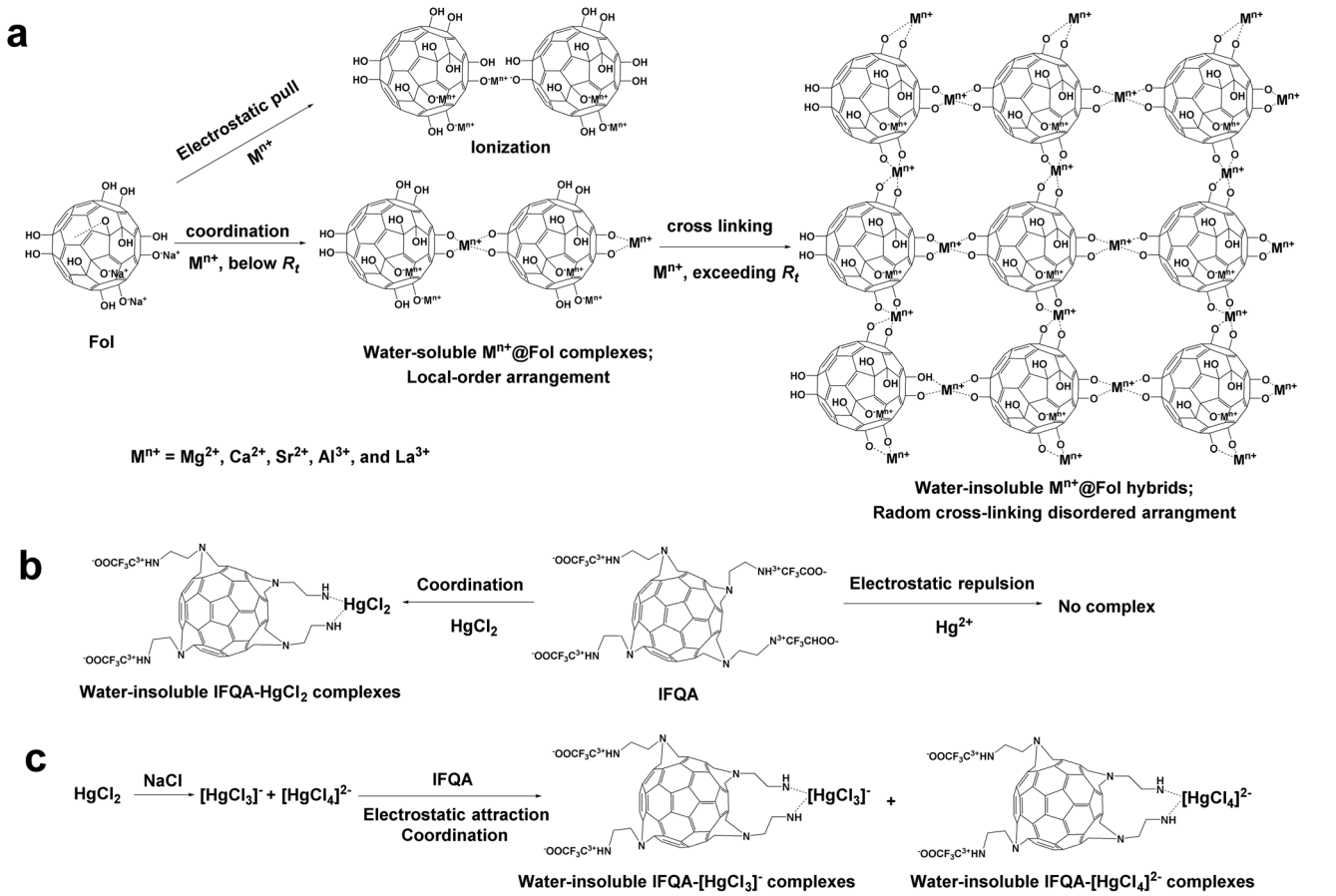

Fig. 10 The scheme of the mode of actions to drive metal-containing ions and water-soluble derivatives of fullerenes for complexation. (a) MCl_n–**FoI** solutions; (b) $HgCl_2$–**IFQA** solution; (c) $HgCl_2$–NaCl–**IFQA** solution.

electrostatic and coordination dual-actuation interactions (Fig. 10a).

On the other hand, cationic **IFQA** did not bind metal cations that lead to precipitation due to the interaction of electrostatic repulsion, which was opposite to **FoI** (Fig. 4, S6 and S7†). For example, the electrostatic repulsion between **IFQA** and Hg^{2+} drove them away from each other, resulting in the inability of coordination to combine into complexes (Fig. 10b). However, after adding more than 500-fold equivalent amount of $HgCl_2$ into **IFQA**, the unexpected generation of the $HgCl_2$–**IFQA** complex could be mainly driven by coordination (Fig. 10b), which is attributed to the weak electrolyte property of mercuric chloride that results in it being dominantly formed as $HgCl_2$ molecules rather than Hg^{2+} ions (<3%) in aqueous solutions.[42,43] Moreover, the insoluble hybrids were observed to fall out of solution when **IFQA** was added into the solution containing metal anions. As shown in Fig. 11, **IFQA** was treated using 20-fold equivalent amount of $HgCl_2$ without a noticeable change in the UV-absorption value and color of the supernatant in comparison to **IFQA**. Interestingly, it has a distinct reduction when it was treated upon the addition of 20-fold $HgCl_2$ and 200-fold NaCl. The sufficient difference in the color of the supernatants made it possible to observe the formation of the brown-colored precipitate after adding NaCl. This phenomenon can also continue to be explained by attractive static-electric force and coordination actions (Fig. 10c). The sufficiently stable $[HgCl_3]^-$ and $[HgCl_4]^{2-}$ can be simultaneously formed in the presence of an excess amount of Cl^- in $HgCl_2$ solution,[43] which turned into electrostatic attractions between anions containing mercury and **IFQA**. These anions will be attached to cationic **IFQA** and subsequently, it can possibly lead to the generation of the water-insoluble $[HgCl_3]^-$–**IFQA** and/or $[HgCl_4]^{2-}$–**IFQA**

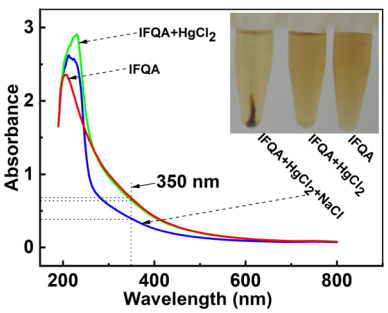

Fig. 11 The photographs of aqueous solution of **IFQA** (0.2 mM) and **IFQA** in the presence of $HgCl_2$ (4.0 mM) without and with NaCl (40 mM) in plastic centrifuge tubes after centrifuging, and the UV-visible spectra of the 5-fold dilution for their supernatants were recorded.

coordinated complexes. In this case, electrostatic attraction continued to play a significant role in the fabrication of **IFQA**-coordination complexes. **IFQA**, as cationic fullerene ligands, can also chelate metal anions to form metal ion–fullerene complexes, but the prerequisite is that free metal cations must firstly be converted into the anionic form. Conversely, **IFQA** cannot directly form complexes with free metal cations in solution, or rather, metal cations cannot induce the further assembly of **IFQA**. It indirectly suggested that electrostatic attraction also mediated the further assembly of **FoI** by metal cations. It can be evaluated from the relevance and competence with the surface charge and structure of polyhydroxy functional groups that **FoI** can provide a good opportunity for coordinating "naked" metal cations to discover novel metal ion–fullerenol complexes.

The best condition for the fabrication of water-soluble M^{n+}@**FoI** coordination complexes appeared when the concentration ratio was close to R_t. This, in principle, led to better discrimination for the formation of insoluble hybrids from water-soluble complexes and a subsequent increase in the preparation efficiency to harvest a water-soluble product. Thus, the judicious choice of the ratio of **FoI** and appropriate salts, as close to, but not exceeding, R_t as possible, resulted in the invention of the procedures, allowing the suppression of the formation of insoluble cross-linking hybrids and leaving water-soluble and locally-ordered microstructural M^{n+}@**FoI** complexes as the majority of products. Furthermore, coordination effects were directly validated in XPS spectra showing the metal cation and oxygen binding feature (Fig. 7(a3)–(e3)). Thus, the most likely way for water-soluble M^{n+}@**FoI** formation is dual-actuation mode by electrostatic and coordination actions. Such M^{n+}@**FoI** complexes with variable morphologies may be stable enough to survive in normal aqueous environments.

At the present stage, the multi-valent metallic cation-induced self-assembly of **FoI** to obtain the water-soluble M^{n+}@**FoI** complexes was demonstrated. Some paramagnetic metal ions, such as Gd^{3+}, Fe^{3+}, and Mn^{2+}, could also direct the assembly of **FoI** to produce paramagnetic NPs, which will be an interesting candidate as the next generation of fullerene-based MRI contrast agents with high relaxivity. The preparation and testing relaxation property of water-soluble and paramagnetic Gd^{3+}@**FoI**, Mn^{2+}@**FoI**, and Fe^{3+}@**FoI** are ongoing projects. Furthermore, their structure–function relationship will be reported separately in the near future as well to help us understand their relaxivity mechanism for potential MRI applications in biomedical fields.

4 Conclusion

The foregoing results demonstrated that the modulation of the ratio of **FoI** to metal cations enabled the significant reduction of the inevitable complexation to insoluble and random cross-linking hybrids and stabilization of M^{n+}@**FoI** in aqueous solution, leading to a new class of water–soluble metal ion–nanocluster complexes. This idea opens a new opportunity for developing a preparation strategy to fabricate the water–soluble metal cation–fullerenol coordination complexes with merits of versatility, simplicity, convenience, high efficiency, and less loss of time. In future studies, finding new anionic water–soluble fullerene-based ligands will continue to be the core of fabricating water–soluble metal cation–fullerene complexes for potential applications in biomedical fields.

Author contributions

He R. conceived the study, carried out some experiments, and wrote the manuscript; Fan C. carried out the experiments and prepared some parts of the manuscript; Liang Q. took part in some of the experiments; Wang Y. and Gao Y. contributed to nanomaterial preparation; Wu J. analyzed the data; Wu Q. interpreted the results, contributed to nanomaterial characterization and manuscript preparation, and supervised the project; Tai F. designed the experiments and supervised the project.

Conflicts of interest

The authors declare that they have no conflict interest.

Acknowledgements

The authors acknowledge the financial supports of the Natural Science Foundation of Henan Province, China (222300420461, 162300410154), the Key Scientific Research Project of Henan Higher Education Institutions of Henan Province, China (22B210003), and the Special Innovation Project and PhD Start-up Fund of Henan Agricultural University, China (KJCX2020C02, 30500458).

References

1 Z. Wang, Y. Zou, Y. W. Li and Y. Y. Cheng, *Small*, 2020, **16**, 1907042.
2 J. J. Zhou, H. Y. Han and J. W. Liu, *Nano Res.*, 2022, **15**, 71–84.
3 M. X. Wu and Y. W. Yang, *Adv. Mater.*, 2017, **29**, 1606134.
4 H. L. Zhang, A. Li, K. Li, Z. P. Wang, X. C. Xu, Y. X. Wang, M. V. Sheridan, H. S. Hu, C. Xu, E. V. Alekseev, Z. Y. Zhang, P. Yan, K. C. Cao, Z. F. Chai, T. E. Albrecht-Schonzart and S. Wang, *Nature*, 2023, **616**, 482–487.
5 J. G. Du and G. Jiang, *Dalton Trans.*, 2022, **51**, 5118–5126.
6 R. Sitko, M. Musielak, M. Serda, E. Talik, A. Gagor, B. Zawisza and M. Malecka, *Sep. Purif. Technol.*, 2021, **277**, e119450.
7 Y. M. Lin, Z. Z. Qiu, D. Z. Li, S. Ullah, Y. Hai, H. L. Xin, W. D. Liao, B. Yang, H. S. Fan, J. Xu and C. Z. Zhu, *Energy Storage Mater.*, 2018, **11**, 67–74.
8 L. Jiao, Y. Wang, H. L. Jiang and Q. Xu, *Adv. Mater.*, 2018, **30**, 1703663.
9 W. Xu, D. Xiang, J. J. Xu, Y. L. Ye, D. Qiu and Z. Z. Yang, *Polym. Chem.*, 2021, **12**, 172–176.
10 H. Hoelzel, S. L. Lee, K. Y. Amsharov, N. Jux, K. Harano, E. Nakamura and D. Lungerich, *Nat. Chem.*, 2023, **15**, 1444–1451.
11 Y. Shu, Q. Y. Ye, T. Dai, Q. Xu and X. Y. Hu, *ACS Sens.*, 2021, **6**, 641–658.

12 Y. Zhang, C.-Y. Sun and L. Lin, *RSC Adv.*, 2023, **13**, 23396–23401.
13 X. Q. Sun, Y. Zhang, J. Q. Li, K. S. Park, K. Han, X. W. Zhou, Y. Xu, J. Nam, J. Xu, X. Y. Shi, L. Wei, Y. L. Lei and J. J. Moon, *Nat. Nanotechnol.*, 2021, **16**, 1260–1270.
14 H. W. Kroto, J. R. Heath, S. C. O'Brien, R. F. Curl and R. E. Smalley, *Nature*, 1985, **318**, 162–163.
15 T. T. Wang and H. P. Zeng, *Chin. J. Org. Chem.*, 2008, **28**, 1303–1312.
16 A. A. Popov, S. F. Yang and L. Dunsch, *Chem. Rev.*, 2013, **113**, 5989–6113.
17 J. J. Wang, Y. R. Yao, S. T. Yang, X. Y. Zhou, A. Yu, P. Peng and F. F. Li, *Nanomaterials*, 2022, **12**, e1314.
18 T. Habicher, J. F. Nierengarten, V. Gramlich and F. Diederich, *Angew. Chem., Int. Ed.*, 1998, **37**, 1916–1919.
19 J. Fan, Y. Wang, A. J. Blake, C. Wilson, E. S. Davies, A. N. Khlobystov and M. Schroder, *Angew. Chem., Int. Ed.*, 2007, **46**, 8013–8016.
20 C. H. Chen, A. Aghabali, C. Suarez, M. M. Olmstead, A. L. Balch and L. Echegoyen, *Chem. Commun.*, 2015, **51**, 6489–6492.
21 P. Peng, F. F. Li, V. S. P. K. Neti, A. J. Metta-Magana and L. Echegoyen, *Angew. Chem., Int. Ed.*, 2014, **53**, 160–163.
22 A. Kraft, P. Roth, D. Schmidt, J. Stangl, K. Muller-Buschbaum and F. Beuerle, *Chem.–Eur. J.*, 2016, **22**, 5982–5987.
23 X. Y. Zhang, H. L. Cong, B. Yu and Q. Chen, *Mini-Rev. Org. Chem.*, 2019, **16**, 92–99.
24 M. J. Chen, K. Y. Yin, G. P. Zhang, H. Z. Liu, B. Ning, Y. Y. Dai, X. J. Wang, H. G. Li and J. C. Hao, *ACS Appl. Bio Mater.*, 2020, **3**, 358–368.
25 K. N. Semenov and N. A. Charykov, *Russ. J. Phys. Chem.*, 2012, **86**, 1636–1638.
26 K. N. Semenov, N. A. Charykov, V. A. Keskinov, A. S. Kritchenkov and I. V. Murin, *Ind. Eng. Chem. Res.*, 2013, **52**, 16095–16100.
27 V. A. Keskinov, K. N. Semenov, T. S. Gol'tsov, N. A. Charykov, N. E. Podol'skii, A. V. Kurilenko, Z. K. Shaimardanov, B. K. Shaimardanova and N. A. Kulenova, *Russ. J. Phys. Chem.*, 2019, **93**, 2555–2558.
28 N. A. Charykov, V. A. Keskinov, K. A. Tsvetkov, A. Kanbar, K. N. Semenov, L. V. Gerasimova, Z. K. Shaimardanov, B. K. Shaimardanova and N. A. Kulenova, *Processes*, 2021, **9**, 349.
29 G. O. Yur'ev, V. A. Keskinov, K. N. Semenov and N. A. Charykov, *Russ. J. Phys. Chem.*, 2017, **91**, 797–799.
30 R. Anderson and A. R. Barron, *J. Am. Chem. Soc.*, 2005, **127**, 10458–10459.
31 J. Heimann, L. Morrow, R. E. Anderson and A. R. Barron, *Dalton Trans.*, 2015, **44**, 4380–4388.
32 J. R. Li, M. J. Chen, S. D. Hou, L. Y. Zhao, T. Y. Zhang, A. N. Jiang, H. G. Li and J. C. Hao, *Carbon*, 2022, **191**, 555–562.
33 M. Seke, D. Petrovic, M. L. Borovic, I. Borisev, M. Novakovic, Z. Rakocevic and A. Djordjevic, *J. Nanopart. Res.*, 2019, **21**, 239.
34 A. V. Zhilenkov, E. A. Khakina, P. A. Troshin, I. F. Karimov and D. G. Deryabin, *Pharm. Chem. J.*, 2019, **53**, 312–317.
35 Y. J. Liu, T. T. Wang, J. H. Cao, Z. F. Zang, Q. N. Wu, H. Z. Wang, F. J. Tai and R. He, *J. Agric. Food Chem.*, 2019, **67**, 13509–13517.
36 L. O. Husebo, B. Sitharaman, K. Furukawa, T. Kato and L. J. Wilson, *J. Am. Chem. Soc.*, 2004, **126**, 12055–12064.
37 F. F. Wang, N. Li, D. Tian, G. F. Xia and N. Xiao, *ACS Nano*, 2010, **4**, 5565–5572.
38 F. Y. Liu, F. X. Xiong, Y. K. Fan, J. Li, H. Z. Wang, G. M. Xing, F. M. Yan, F. J. Tai and R. He, *J. Nanopart. Res.*, 2016, **18**, 338.
39 J. Wan, J. X. Ma, Y. Y. Zhang, Y. X. Xia, L. Hong and C. Yang, *New J. Chem.*, 2021, **45**, 17660–17666.
40 D. Fati, V. Leeman, Y. V. Vasil'ev, T. Drewello, B. Leyh and H. Hungerbuhler, *J. Am. Soc. Mass Spectrom.*, 2002, **13**, 1448–1458.
41 F. J. Tai, S. Wang, B. S. Liang, Y. Li, J. K. Wu, C. J. Fan, X. L. Hu, H. Z. Wang, R. He and W. Wang, *J. Nanobiotechnol.*, 2022, **20**, 15.
42 J. G. Speight, *Lange's Handbook of Chemistry*, McGraw-Hill, New York, 16th edn, 2005, pp. 1358–1362.
43 S. R. Labhade and K. R. Labhade, *Asian J. Chem.*, 2021, **33**, 2069–2072.
44 Z. C. Xin, Y. T. Shen, H. Hao, L. N. Zhang, X. X. Hu and J. Wang, *Colloids Surf., B*, 2022, **218**, 112776.
45 J. Liu, R. L. Zhu, T. Y. Xu, M. W. Laipan, Y. P. Zhu, Q. Zhou, J. X. Zhu and H. P. He, *J. Environ. Sci.*, 2018, **64**, 1–9.
46 B. Sitharaman, R. D. Bolskar, I. Rusakova and L. J. Wilson, *Nano Lett.*, 2004, **4**, 2373–2378.